Visibility guided phase contrast denoising

Brandon Nelson[a,b*], Thomas Koenig[b,c], Elisabeth Shanblatt[a], Shuai Leng[a,b], Cynthia McCollough[a,b]

[a] Department of Radiology, Mayo Clinic, Rochester, MN 55905
[b] Graduate Program in Biomedical Engineering and Physiology, Mayo Clinic Graduate School of Biomedical Sciences, Rochester, MN 55905
[c] Ziehm Imaging, Donaustr. 31, 90451 Nuremberg, Germany

ABSTRACT

Talbot-Lau grating interferometry enables the use of clinical x-ray tubes for phase contrast imaging, greatly broadening its utility for both laboratory and preclinical applications. However, phase contrast measurements made in porous or highly heterogeneous media are negatively impacted by low visibility, the interferometer signal amplitude used to calculate relative phase shifts. While this loss in visibility is the source of dark field contrast it presents an additional source of noise in phase images. In this work, we develop a method to use normalized visibility images as the weighting matrix for denoising the corresponding phase contrast images. By using the visibility to guide filtering, the resulting denoised images are locally smoothed in regions of low visibility while maintaining spatial detail in regions of high visibility. This work demonstrates how the complementary properties of the dark field signal in grating interferometry can be leveraged to improve image quality in phase contrast images and presents an application in preclinical lung micro-CT.

Keywords: Phase contrast, denoising, dark field, lung, micro-CT

1. INTRODUCTION

1.1 Purpose

The purpose of this study was to reduce low-visibility induced noise in phase contrast images acquired via Talbot-Lau grating interferometry using the corresponding visibility contrast as a weighting matrix to guide denoising strength. Such a method uses the relationship between phase and normalized visibility contrast images where regions of low normalized visibility indicate additional low-visibility noise in the phase channel. By using the normalized visibility image as a map for preferentially denoising low visibility areas in phase contrast regions, spatial resolution is maintained in adjacent high visibility regions. This type of guided denoising is most appreciable in imaging of media with highly heterogeneous visibility such as seen in lung imaging, an area that could potentially benefit from phase contrast imaging.

1.2 Background

In conventional x-ray imaging, noise originates primarily from quantum mottle due to limitations in photon flux and electronic noise and is propagated through reconstruction processes[1]. Noise in phase contrast images acquired via grating interferometry additionally can come from instabilities in the phase stepping procedure[2] and from unresolvable intra-pixel phase gradients and other systematic factors[3,4]. This last source of noise in phase contrast is a sampling artifact that reduces the measured Talbot carpet visibility V and contributes to the normalized-visibility signal. Previous studies[5] have shown that this low visibility noise has a systematic (i.e. deterministic) origin, and cannot be reduced by increasing radiation dose.

Grating interferometer-based phase contrast imaging simultaneously generates three co-registered image contrasts: 1.) absorption, 2.) differential phase, and 3.) normalized visibility, and previous work has explored how these signals can be combined to accentuate different sample properties, finding application in phase contrast mammography[7,8]. This work presents the first application to take advantage of the relationship between grating interferometer contrasts for denoising purposes, in particular the relationship between normalized visibility and low-visibility phase noise. Here we explore using normalized visibility as an indicator of low-visibility phase noise, which, as stated previously, is distinct from quantum noise and electronic noise, and using it as a guide for denoising our phase contrast channel. In this paper we make the distinction that dark field contrast[9] is dependent on the small-angle-scattering properties of the sample, while normalized visibility contains both dark field and signal from additional systematic bias stated previously[3-5].

*nelson.brandon@mayo.edu;

In addition to its enhanced soft tissue contrast properties compared to traditional absorption contrast[10-12], phase contrast has also been shown to have noise properties supporting its use in high resolution imaging of fine structures[6,13]. Thus we justify that our proposed technique of using normalized visibility as a guide for denoising phase will enable future high resolution phase imaging by mitigating the effects of low-visibility phase noise encountered by unresolvable steep phase gradients or underlying scattering media. We have identified that preclinical lung imaging is one such area that could benefit from our proposed visibility guided phase denoising technique. This is because thoracic anatomy varies greatly between the mostly homogenous mediastinum to the heterogeneous lungs containing adjacent regions of high and low visibility[14-16]. In the lung large structures like blood vessels, bronchial walls, and dense interstitial tissue are juxtaposed with sub-resolvable small airways which generate strong visibility contrast, consequently adding low-visibility noise in the phase channel, thus obscuring nearby larger structures.

Micro-CT is already a powerful tool in preclinical lung studies where in-vivo systems enable longitudinal monitoring of disease[17,18] as well as high resolution non-destructive imaging of morphology[19]. However, despite its success, traditional micro-CT suffers from many of the same challenges of clinical CT for diagnosing diffuse lung diseases. In particular, poor soft tissue contrast limits sensitivity to early stages of disease, which are often presented as ground-glass opacifications, or subtle regional increases in attenuation due to fluid or interstitial tissue accumulation[20]. The improved soft tissue contrast and additional information offered by x-ray phase and dark field contrasts could benefit this field of preclinical lung imaging. However, full utilization of phase contrast properties will require engineering approaches to overcome the challenges of imaging materials with highly heterogeneous visibility. In this work we present a push in this direction with a method for reducing low-visibility phase noise using normalized visibility as a guide and introduce its potential application in lung imaging.

2. METHODS

2.1 Grating Interferometry

Grating interferometry-based x-ray phase contrast uses a phase shifting grating (G1) in a beam of partially coherent x-rays to create a Talbot carpet interference pattern that, at specific Talbot distances, has periodic intensity variations. This intensity pattern can thus encode phase shifts induced by a sample placed in the beam line into changes in intensity. However, while maintaining compact geometries, the resulting period of these intensity variations is too small to be resolved on most detectors, so multiple periods are sampled simultaneously with a second absorption grating (G2) placed downstream of the phase grating. Stepping these gratings relative to each other samples the Talbot carpet and generates a phase stepping curve. After placing an object (*obj*) in the beam, the change in the intensity oscillations from the object free reference stepping (*ref*) is used to generate three image contrasts via a homodyne process using the Fast Fourier transform.

The conventional transmission image is generated from the change in attenuation baseline as given by the amplitude of the zeroth order Fourier coefficient a_0, $T = a_{0,obj}/a_{0,ref}$. Next, the differential phase comes from the difference in phases of the first order Fourier coefficients of the sampled Talbot carpet period, $\Delta\phi = \phi_{1,obj} - \phi_{1,ref}$. This spatial derivative of the phase in the stepping direction is what is directly measured in grating interferometry. Full phase images of the object can then be generated by integrating the projections in the same stepping direction or via CT reconstruction using a Hilbert filter[9]. Visibility V is a measure of the relative strength of the first-order intensity variations a_1 relative to the baseline intensity a_0. In terms of Fourier coefficients it is calculated as $V = \frac{2a_1}{a_0}$, and also serves as a proxy for image quality in differential phase contrast images. Normalizing the measured visibility of the sampled object with respect to the reference background image yields the third contrast, normalized visibility $V_{norm} = V_{obj}/V_{ref}$. For a more complete description of grating interferometry, see references[9,21].

2.2 Visibility guided phase denoising method

Our developed denoising method leverages the fact that the V_{norm} image gives a normalized pixel map of differential phase contrast $\Delta\phi$ image quality with a known relationship to noise[6], thus we use the complement 1-V_{norm} (otherwise known as dark field contrast when accounting for only small-angle scatter events) which serves as the base of our weighting matrix w that we use to guide denoising. While this introduced principal can be applied to either differential phase projections or integrated reconstructed CT images, in this work we start with the image based

approach, taking advantage of higher contrast at material interfaces and improving the edge preservation of the method, important in high resolution imaging.

The denoising technique starts with generating a copy of the original phase CT image for filtering, here called ϕ_{filt}. By using the normalized visibility contrast as the core of our denoising technique scattering material generating dark field will be flagged for denoising as well as steep phase gradients at sharp edges that reduce normalized visibility as well. To prevent smoothing of sharp edges an edge-preserving filtering technique is used to generate ϕ_{filt}. Our choice of filter was a nonlocal means (NLM) filter implemented in Matlab (Matlab and Image Processing Toolbox release 2018b The MathWorks, Inc., Natick, Massachusetts, United States) using a search window of radius 25 pixels and comparison window of 17 pixel radius and a smoothing factor of 50 in 1024x1024 image matrices. These parameters were determined empirically based on best smoothing appearance while preserving edges but can be tuned based on the application. Previous work[22] has shown the effectiveness of NLM image-based noise reduction in clinical CT while preserving edges.

After generating ϕ_{filt}, the local contribution of this strongly filtered image is determined via the weighting matrix w,

$$w_{i,j} = \begin{cases} (1 - V_{norm_{i,j}})^{1/p}, & 1 - V_{norm_{i,j}} \geq t \\ 0, & 1 - V_{norm_{i,j}} < t \end{cases} \tag{1}$$

where $p > 0$ is a scalar parameter used to increase the strength of denoising, i, j are matrix element indices, and t is an additional parameter used to set a minimum threshold to further control edge preservation in addition to the ϕ_{filt} filter choice. The threshold t is set knowing that $V_{norm_{i,j}} > 1 - t$, contains regions considered as high fidelity, not being flagged for denoising. The weighting matrix w is then used to create a linear combination of the original unfiltered phase contrast image ϕ, with filtered copy, ϕ_{filt}, yielding the final denoised image $\phi_{denoised}$,

$$\phi_{i,j_{denoised}} = (1 - w_{i,j})\phi_{i,j} + w_{i,j}\phi_{i,j_{filt}}. \tag{2}$$

2.3 Phantom study

We first demonstrate our method using a cylindrical acrylic phantom with 6 air inserts and a wooden toothpick insert to generate a low visibility region. Wood has been shown previously to generate dark field signal due to its fibrous and heterogeneous structure[23]. Data were acquired on a tabletop Talbot-Lau grating interferometer to generate absorption, differential phase, and dark field images employing a 1st Talbot order grating geometry using a 40 keV effective energy with a G0-G1 distance of 52.2 cm and G1-G2 distance of 25.1 cm. The gratings G0, G1, and G2 had respective periods of 10, 3.24, and 4.8 μm. A PANalytical XRD C-tech source with 400 μm x 800 μm focal spot size was operated at 55 kVp and 35 mA with no additional filtration at an approximate 10 degree anode angle. The camera was a Princeton instruments PIXIS 2048F binned to 2x2, amounting to an effective pixel pitch of 52 μm. Six steps over one period were acquired. The mean reference visibility was $V_{ref} = 21\%$.

A computed tomographic image set was acquired with exposure times of 2.4 seconds per phase step over 6 steps, with absorption, $\Delta\phi$, and V_{norm} projections acquired at 0.25 degree increments over a 360 degree range. Absorption, integrated differential phase ϕ, and $1 - V_{norm}$ projections were then all reconstructed into three separate image sets using an FDK filtered back projection algorithm. The absorption and phase reconstructed image sets were converted to standard Hounsfield Units (HU) and phase contrast Hounsfield Units (HU-P)[12,23], respectively, while the $1 - V_{norm}$ reconstructed image set was normalized relative to the maximum and minimum measured image values. This last normalization step is optional and is done out of convenience in selecting an appropriate threshold parameter t. The resulting ϕ and normalized $1 - V_{norm}$ image sets were then used in the denoising algorithm as described in equations (1) and (2).

2.4 *Ex vivo* lung preparation

To demonstrate the applicability of our visibility guided denoising method, a set of air inflated dried mouse lungs were imaged and denoised using our described technique. The lungs came from a wild type, B6 mouse that was humanely sacrificed for another experiment. The lungs were surgically removed, cannulated and instilled with a fixation solution of 50% PEG 400, 25% Ethyl alcohol, 10% formaldehyde and 15% water to a filling pressure of a 20 cm water

column. The lungs were tied off at the trachea and immersed in the same solution for 7 days before being air inflated at 25 mmHg and dried for 72 hours[24]. This fixation method preserves native air-tissue contrast and the inflated structure of the lung, but comes at the cost of losing the liquid surfactant layer that covers the airways. It is a standard method for *ex vivo* structural imaging as laid out by the American Thoracic Society guide on structural lung imaging[25].

3. RESULTS

3.1 Phantom study

Figure 1A-C shows the original 3 contrast reconstructed images pertaining to the phantom study, ϕ, absorption, and $1 - V_{norm}$ respectively. Directly besides the $1 - V_{norm}$ panel in Figure 1D is the weighting matrix w, from equation (1). By setting a threshold of $t = 0.4$, any pixels with a visibility > 0.6 are excluded from filtering. By setting this threshold high enough the air-acrylic edges in Figure 1C are spared from the filtering matrix in Figure 1D, and those non-zero elements of w are then weighted further with a denoising strength parameter of $p = 4$. This weighting matrix w then controls the local weighting strength of the strongly filtered NLM copy ϕ_{filt} in Figure 1E, to give the final visibility guided denoised output $\phi_{denoised}$ in Figure 1F. A qualitative comparison between ϕ, ϕ_{filt}, and $\phi_{denoised}$ in Figure 1A, E, and F shows an increase in conspicuity of the different wood grains in the insert in both ϕ_{filt} and $\phi_{denoised}$, while $\phi_{denoised}$ avoids over-smoothing the acrylic background and air-acrylic interfaces.
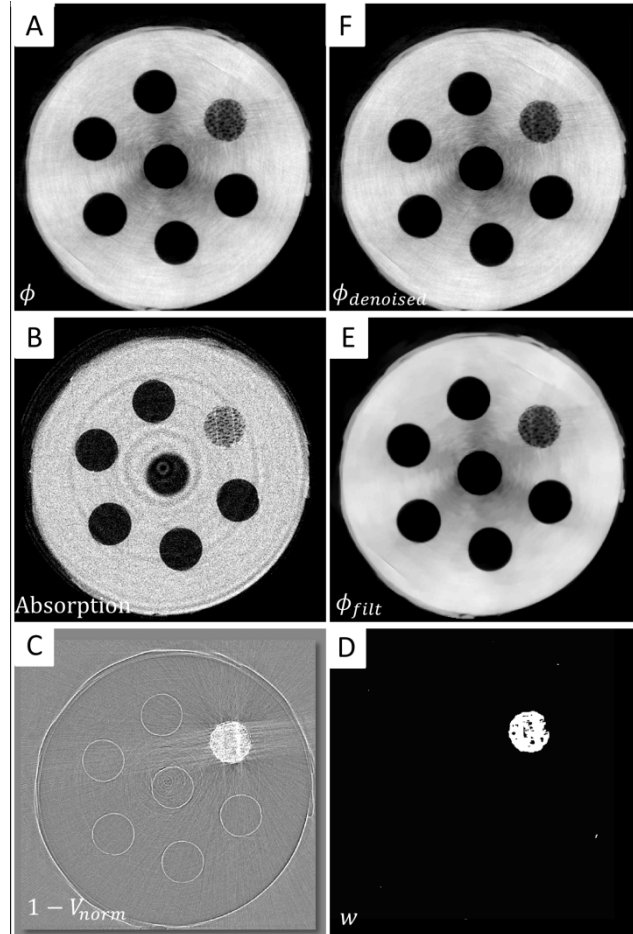
Figure 1: Visibility guided phase denoising method. A.) The original phase reconstructed image ϕ with display settings W/L = 1000/0 HU-P. B.) Absorption reconstructed image, W/L = 1000/0 HU. C.) Normalized $1 - V_{norm}$ image W/L = 0.6/0.2. D.) weighting matrix w with threshold $t = 0.4$ and denoising strength $p = 4$. E.) NLM filtered ϕ_{filt}. F.) Denoised output, $\phi_{denoised}$.

A closer look at the wooden insert and the effects of increasing the denoising parameter p are explored in Figure 2. The top row contained in Figure 2A shows increasing filtration strength from no filtration ϕ, up to $p = 16$, followed by the globally filtered NLM copy ϕ_{filt}. Black arrows in Figure 2A point out subtle regions of increased phase signal in the wood that becomes more apparent following denoising. Selection of p can control over-smoothing of darker wood grains. Figure 2B shows the qualitative effect of increasing the denoising parameter by showing the difference image $\phi_{denoised} - \phi$ for each value of p shown. Note in the ϕ_{filt} panel of Figure 2B that some edges are preserved via NLM, but by setting a sufficient threshold t, further edge-preservation is enforced. Figure 2C then shows the quantitative noise reduction as a function p, generated by measuring the standard deviation within the box ROI (Figure 2A) for each strength p, σ_{ϕ_p}, and comparing against the standard deviation of the original noisy image σ_ϕ. Note that the shape of the curve is the result of our choice of setting p as fractional exponent in equation (2) such that the denoising strength quickly saturates to an approximately 33% noise reduction as reflected in Figure 2C.
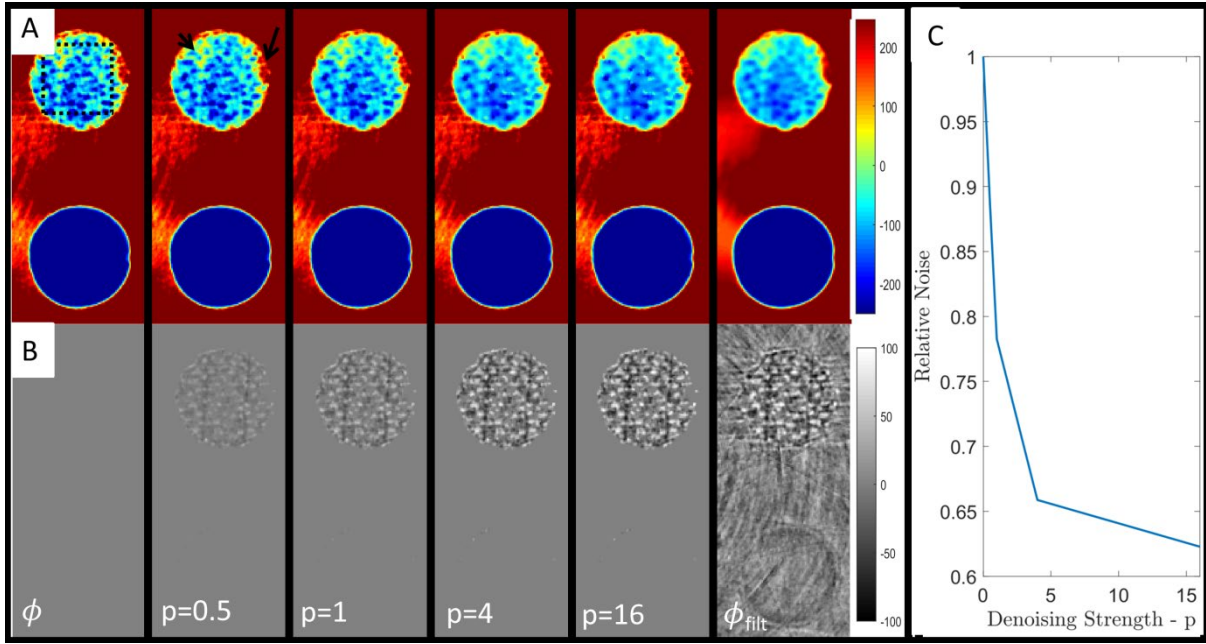
Figure 2: Effect of denoising strength parameter p. Row A.) Shows a close-up view of the wood and air inserts in the acrylic cylinder phantom from Figure 1 denoised at increasing strengths p, W/L = 500/0 HU-P. Arrows draw attention to subtle changes in phase contrast, easily obscured by noise. Row B.) Shows the corresponding difference image $\phi_{denoised} - \phi$, W/L = 200/0 HU-P. Panel C.) plots the relative noise $(\sigma_{\phi_p}/\sigma_\phi)$ in the wooden insert, measured within the box ROI, as a function of p.

3.2 Ex vivo fixed lung study

Next, we present a preclinical lung imaging application of our image-based visibility guided denoising method in Figure 3. The whole mouse lung sample is shown outside of the thoracic cavity with the heart embedded. The sample is dried and inflated to maintain natural air-tissue contrast at an end-inspiration inflation volume and imaged at 52 μm isotropic voxels. An axial slice at the level of the heart is shown and major structures of large cartilage-lined airways and blood vessels are visible in the lung against the diffuse background of unresolvable small airways. Figure 3A-C shows the original phase ϕ, absorption, and $1 - V_{norm}$ reconstructed images. Note how homogenous structures of the heart, large bronchi, and resolvable vessels are dark in the $1 - V_{norm}$ image causing them to be naturally excluded. Setting a threshold of t=0.4 further preserves some vessels at the edge of the systems resolving power as shown in the Figure 3D weighting matrix w. The NLM filtered copy ϕ_{filt} and final visibility guided denoised output $\phi_{denoised}$ follow in Figure 3E-F. Attention can be drawn to the interstitial tissue connecting large bronchi and vessels that are of intermediate intensity between bright vessels and the darker lung background. Shown at the same display settings these connective structures are more conspicuous against the filtered background in ϕ_{filt} and $\phi_{denoised}$ while the sharpness of adjacent airway walls and vessels is preserved in $\phi_{denoised}$.
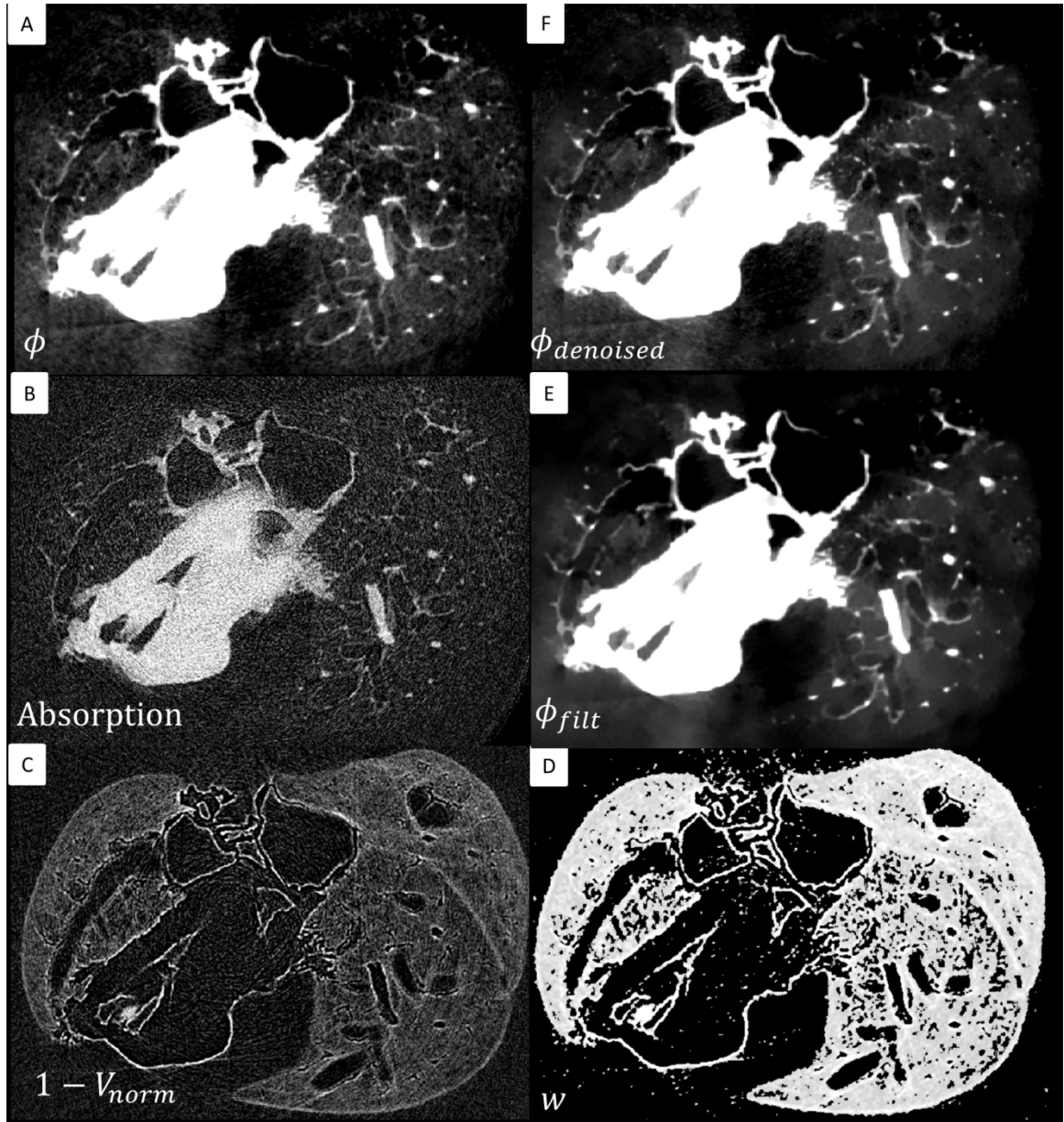
Figure 3: Application of visibility guided phase denoising in a preclinical lung sample: shown here, axial images of a mouse lung with embedded heart. A). Original phase reconstructed image ϕ with display settings W/L = 1000/-400 HU-P. B.) Absorption reconstructed image, W/L = 1000/-300 HU. C.) Normalized $1 - V_{norm}$ image W/L = 1/0.5. D.) weighting matrix w with threshold $t = 0.4$ and denoising strength $p = 4$. E.) NLM filtered ϕ_{filt}. F.) Denoised output W/L = 1000/-400 HU-P.

This effect of increased conspicuity of connective tissues can be more clearly seen in Figure 4 which shows a close-up view of a lower right region of the lung slice shown in Figure 3. Figure 4A-C shows a close-up view of the same ϕ, ϕ_{filt}, and output $\phi_{denoised}$ images, against the absorption image in Figure 4D. Again, qualitatively these low intensity interstitial structures standout more in the filtered images, and this is shown quantitatively in Figure 4E by measuring the CNR of the interstitial tissue ROI boxed in Figure 4A as a function of denoising strength p. The CNR increases with p before reaching a maximum due to the saturation of the denoising strength as discussed previously. Figure 4F then demonstrates the edge preservation of the method by plotting the line profile shown in Figure 4B at different p denoising

strengths and against ϕ_{filt} and absorption. Despite NLM being an edge-preserving filtering method, some of the vessel peak is smoothed, but by omitting it from filtration with the set threshold of $t = 0.4$, the edge is better preserved.
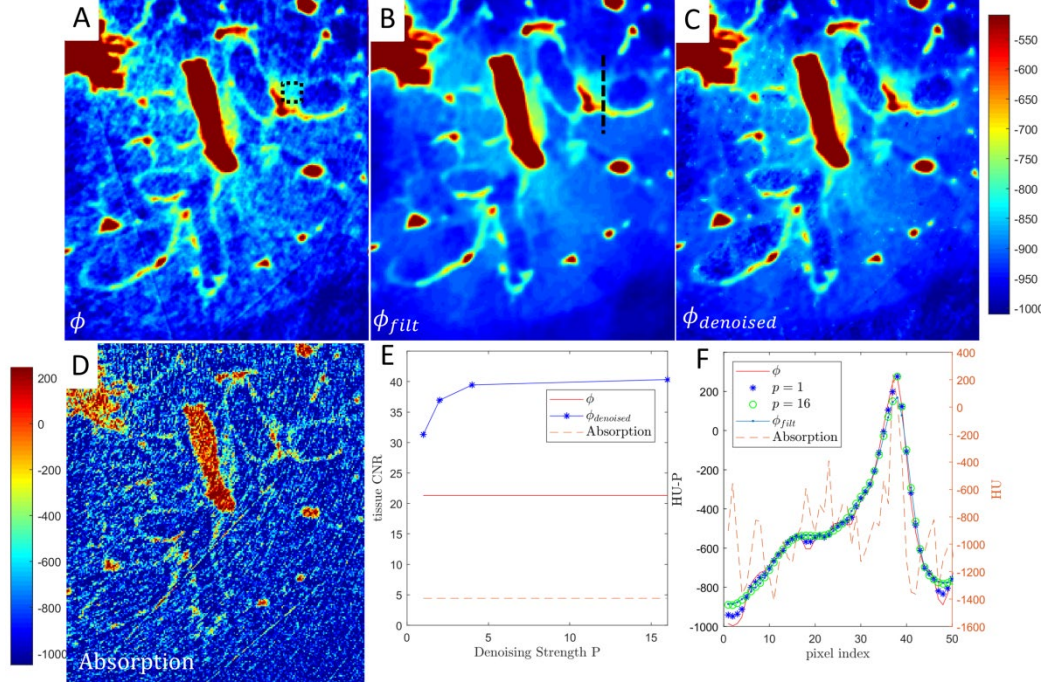
Figure 4: Close-up view of a lung region. A-C) show ϕ, ϕ_{filt}, and output $\phi_{denoised}$ from Figure 3 for qualitative assessment along with D) the absorption image. E) Plotting of CNR as a function of denoising strength p in the ROI shown in A). F) Line profile from B) comparing the noise reduction and edge preservation between ϕ, two denoising strengths, ϕ_{filt}, and the absorption image.

4. DISCUSSION

X-ray Talbot-Lau grating interferometry offers unique phase and normalized visibility contrasts on top of absorption measurements that can be implemented on standard x-ray tubes and detectors. With commercial systems recently made available[26], grating-based phase contrast is now accessible to biomedical researchers to further pursue applications. In this work we have demonstrated one such application in preclinical lung imaging as well as the challenge brought about by phase contrast imaging of porous and scattering media as seen in the lungs. Importantly, we introduce and explore one solution that utilizes the relationship between the normalized visibility and phase contrasts that the first provides an image quality map of the second, a map of deterministic noise introduced at low visibilities. Our method can selectively denoise regions of low visibility, while preserving high-visibility regions and edges above a minimum visibility threshold of $1 - t$ as shown in Figure 1.

One limitation in our method is that our NLM filtering method to generate ϕ_{filt} is a smoothing filter which does not adequately account for the low frequency noise texture of phase contrast[13]. This can be seen in Figure 2, where even the full weight ϕ_{filt} can only achieve a ~30% noise reduction in the wooden insert by smoothing out the higher frequency noise content, which is only a tail of the mostly lower frequency phase noise content. The achieved noise reduction could be greatly enhanced by tailoring a filter for ϕ_{filt} that better accounts for the phase contrast noise properties.

Despite this limitation, our visibility guided phase denoising technique proved effective at enhancing the conspicuity of interstitial connective tissues against the unresolvable small airway lung background while preserving edges as shown in Figures 3-4. These structures are of importance in the monitoring of interstitial lung diseases that currently are the focus of several micro-CT preclinical studies[17-19,27,28] that could potentially benefit from the enhanced soft tissue contrast and low frequency noise characteristics of phase or sub-resolution information in dark field. While

further work remains to identify technique factors that optimize the balance of normalized visibility to extract useful information from both the phase and dark field channels for specific applications, our method provides a solution for reducing the low visibility phase noise in low visibility samples.

5. CONCLUSION

This study demonstrated the use of the normalized visibility image as a weighting matrix to denoise the simultaneously acquired phase contrast image in x-ray Talbot-Lau grating interferometry. This method is an example of using the relationship between different grating interferometer contrasts to improve image quality of one of the contrasts, here using normalized visibility to enhance the phase. In our study we were able to achieve a 30% noise reduction in a wooden insert and a 30% CNR enhancement of a soft tissue ROI while preserving edges. This approach could be used further in preclinical lung imaging or in other porous scattering media to retain phase information.

ACKNOWLEDGEMENTS

6. REFERENCES

[1]   J. Hsieh, *Computed tomography : principles, design, artifacts, and recent advances*, Third edition. ed. Bellingham, Washington, USA: SPIE, 2015, pp. xvii, 639 pages.

[2]   F. Horn *et al.*, "Implementation of a Talbot-Lau interferometer in a clinical-like c-arm setup: A feasibility study," *Sci Rep,* vol. 8, no. 1, p. 2325, Feb 2 2018.

[3]   Y. Yang and X. Tang, "The second-order differential phase contrast and its retrieval for imaging with x-ray Talbot interferometry," *Med Phys,* vol. 39, no. 12, pp. 7237-53, Dec 2012.

[4]   W. Yashiro, D. Noda, and K. Kajiwara, "Effect of insufficient temporal coherence on visibility contrast in X-ray grating interferometry," *Opt Express,* vol. 26, no. 2, pp. 1012-1027, Jan 22 2018.

[5]   T. Koenig *et al.*, "On the origin and nature of the grating interferometric dark-field contrast obtained with low-brilliance x-ray sources," *Phys Med Biol,* vol. 61, no. 9, pp. 3427-42, May 7 2016.

[6]   G. H. Chen, J. Zambelli, K. Li, N. Bevins, and Z. Qi, "Scaling law for noise variance and spatial resolution in differential phase contrast computed tomography," *Med Phys,* vol. 38, no. 2, pp. 584-8, Feb 2011.

[7]   Z. Wang *et al.*, "Image fusion scheme for differential phase contrast mammography," (in English), *Journal of Instrumentation,* vol. 8, Jul 2013.

[8]   F. Scholkmann, V. Revol, R. Kaufmann, H. Baronowski, and C. Kottler, "A new method for fusion, denoising and enhancement of x-ray images retrieved from Talbot-Lau grating interferometry," *Phys Med Biol,* vol. 59, no. 6, pp. 1425-40, Mar 21 2014.

[9]   F. Pfeiffer, T. Weitkamp, O. Bunk, and C. David, "Phase retrieval and differential phase-contrast imaging with low-brilliance X-ray sources," (in English), *Nature Physics,* vol. 2, no. 4, pp. 258-261, Apr 2006.

[10]   T. J. Davis, D. Gao, T. E. Gureyev, A. W. Stevenson, and S. W. Wilkins, "Phase-Contrast Imaging of Weakly Absorbing Materials Using Hard X-Rays," (in English), *Nature,* vol. 373, no. 6515, pp. 595-598, Feb 16 1995.

[11]   M. Bech, T. H. Jensen, R. Feidenhans'l, O. Bunk, C. David, and F. Pfeiffer, "Soft-tissue phase-contrast tomography with an x-ray tube source," (in English), *Physics in Medicine and Biology,* vol. 54, no. 9, pp. 2747-2753, May 7 2009.

[12]   T. Donath *et al.*, "Toward clinical X-ray phase-contrast CT: demonstration of enhanced soft-tissue contrast in human specimen," *Invest Radiol,* vol. 45, no. 7, pp. 445-52, Jul 2010.

[13]   T. Kohler, K. Jurgen Engel, and E. Roessl, "Noise properties of grating-based x-ray phase contrast computed tomography," *Med Phys,* vol. 38 Suppl 1, p. S106, Jul 2011.

[14]   K. Hellbach *et al.*, "X-ray dark-field radiography facilitates the diagnosis of pulmonary fibrosis in a mouse model," *Sci Rep,* vol. 7, no. 1, p. 340, Mar 23 2017.

[15]   K. Scherer *et al.*, "X-ray Dark-field Radiography - In-Vivo Diagnosis of Lung Cancer in Mice," *Sci Rep,* vol. 7, no. 1, p. 402, Mar 24 2017.

[16] A. Yaroshenko *et al.*, "Improved In vivo Assessment of Pulmonary Fibrosis in Mice using X-Ray Dark-Field Radiography," *Sci Rep,* vol. 5, p. 17492, Dec 1 2015.

[17] J. R. Ashton, J. L. West, and C. T. Badea, "In vivo small animal micro-CT using nanoparticle contrast agents," (in English), *Frontiers in Pharmacology,* vol. 6, Nov 4 2015.

[18] K. A. Johnson, "Imaging techniques for small animal imaging models of pulmonary disease: micro-CT," *Toxicol Pathol,* vol. 35, no. 1, pp. 59-64, Jan 2007.

[19] D. M. Vasilescu *et al.*, "Assessment of morphometry of pulmonary acini in mouse lungs by nondestructive imaging using multiscale microcomputed tomography," *Proc Natl Acad Sci U S A,* vol. 109, no. 42, pp. 17105-10, Oct 16 2012.

[20] M. I. Schwarz and T. E. King, *Interstitial lung disease*, 4th ed. Hamilton, Ont. ; Lewiston, N.Y.: B.C. Decker, 2003, pp. x, 941 p.

[21] A. Bravin, P. Coan, and P. Suortti, "X-ray phase-contrast imaging: from pre-clinical applications towards clinics," *Phys Med Biol,* vol. 58, no. 1, pp. R1-35, Jan 7 2013.

[22] Z. Li *et al.*, "Adaptive nonlocal means filtering based on local noise level for CT denoising," *Med Phys,* vol. 41, no. 1, p. 011908, Jan 2014.

[23] M. Bech, O. Bunk, T. Donath, R. Feidenhans'l, C. David, and F. Pfeiffer, "Quantitative x-ray dark-field computed tomography," *Phys Med Biol,* vol. 55, no. 18, pp. 5529-39, Sep 21 2010.

[24] S. A. Groskin and E. R. Heitzman, *Heitzman's the lung, radiologic-pathologic correlations*, 3rd ed. St. Louis: Mosby, 1993, pp. xiv, 636 p.

[25] C. C. Hsia, D. M. Hyde, M. Ochs, E. R. Weibel, and A. E. J. T. F. o. Q. A. o. L. Structure, "An official research policy statement of the American Thoracic Society/European Respiratory Society: standards for quantitative assessment of lung structure," *Am J Respir Crit Care Med,* vol. 181, no. 4, pp. 394-418, Feb 15 2010.

[26] Bruker. (2019, 1/20/2019). *SkyScan 1294*. Available: https://www.bruker.com/products/microtomography/in-vivo-micro/skyscan-1294/overview.html

[27] D. Cavanaugh *et al.*, "Quantification of bleomycin-induced murine lung damage in vivo with micro-computed tomography," *Acad Radiol,* vol. 13, no. 12, pp. 1505-12, Dec 2006.

[28] E. De Langhe *et al.*, "Quantification of Lung Fibrosis and Emphysema in Mice Using Automated Micro-Computed Tomography," (in English), *Plos One,* vol. 7, no. 8, Aug 13 2012.